Characterization and Use of a Novel Laser Scanning Microscope

Alan Chen, Nicholas Diaco, and Adeel Mahmood

School of Applied and Engineering Physics
Cornell University, Ithaca, NY 14853
(Dated: December 11, 2018)

We present the design of a laser scanning microscope system capable of capturing high spatial resolution reflectance measurements. A red diode laser is scanned across a sample surface using a single 2-axis steering mirror controlled by LabVIEW. The reflected light intensity modulates the voltage output from a photodiode-based amplifier circuit. The light-modulated voltage is processed via analog-to-digital conversion to generate a real-time 2D intensity plot. Several parameters including step rate, vertical and horizontal sampling ranges, and sample points per distance are controllable via a LabVIEW GUI, allowing for convenient synchronous scanning and sampling functionality. Our microscope has been successfully tested on several samples to verify its design.

I. INTRODUCTION

Optical imaging and spectroscopy have assumed great importance in numerous fields of research and engineering. In particular, many advances in semiconductor technology and the biological sciences have been precipitated by laser scanning microscopy. A scanning laser microscope operates by scanning a focused laser beam in a raster pattern over a sample of interest. The light reflected off of the sample at any given point hits a light-sensitive surface, where the light intensity is translated to an electrical signal. These signals are aggregated to create a 2D array of pixels that map the sample's reflectivity, providing the user with a high-resolution image. Several variations of this technique, such as using a pinhole to block unfocused light in so-called confocal laser microscopy, are well-documented in the literature [1].

Measurements of reflectance provide insight into many properties of interest in physics. Many such properties, such as resonance, are generally analyzed on a point-by-point basis since no 2D characterization tools are in common use. Resonance effects such as surface plasmon-polaritons (SPPs), as well as localized surface plasmon resonance (LSPR) [2], are regularly employed in applications ranging from tunable directive antennas [3] and nanoparticle-mediated photothermal therapy [4] to efficient meta-couplers [5] and sensing applications. The ability to measure the resonance properties of a sample over a 2D area, as is possible with laser scanning microscopy, could pave the way for applications that are heretofore too complex to characterize.

In addition to its ability to probe physical phenomena, scanning laser microscopy has many well-known advantages in biological research. Confocal fluorescence microscopy, which operates on the principles of scanning laser microscopy, grants users the ability to capture volumetric images of biological tissue [6]. This technique's power lies in its ability to image a region of interest, such as *in vivo* brain vasculature, without interfering data from any surrounding tissue [7]. Furthermore, several groups have achieved sub-diffraction resolution using fluorescent microscopy, capturing images of single molecules and proteins [8]. Unfortunately, however, the major-

ity of fluorescence microscopy practiced today employs complex, expensive optical assemblies that cannot be adjusted by end users.

In this paper, we propose and characterize a laser scanning microscope capable of performing high-precision and spatially resolved measurements of reflectance across a wide sample area. Many previous scanning and imaging systems are based on moving the sample stage, the laser, or both to cover a large area [9]. The former approaches are susceptible to mechanical vibrations, are highly complicated, and allow for less repeatability of measurements and smaller integration times. In our system, the laser spot is moved via a steering mirror by quantized, precise steps of two independently controlled stepper motors. This minimizes the movement of mechanical parts and maximizes stability and repeatability. Furthermore, our proposed laser is comprised entirely of accessible, off-the-shelf parts controlled by a simple GUI, making the microscope's operation both economical and adjustable.

II. DESCRIPTION OF THE SYSTEM

A. Opto-Mechanical Assembly

As shown in Figure 1, the body of the microscope is comprised of a red diode laser, beam splitter, steering mirror, objective lens, and several auxiliary lenses. The laser beam is first expanded and split towards the steering mirror, which in turn reflects the laser light towards the sample. On the optical path towards the sample, a 4F lens system is used to prevent beam walking, followed by an objective lens to focus the light on the sample. Light reflected from the sample returns through the aforementioned microscope elements to the photodiode circuit, where the intensity is converted to an electrical signal and recorded by means of analog-to-digital conversion (ADC).
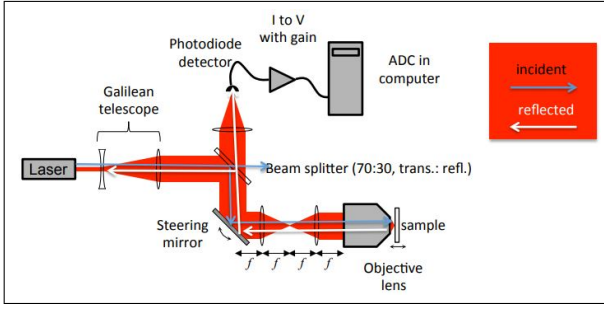
FIG. 1. **Internal microscope setup and external interface:** The steering mirror is used to control the position of the incident laser spot on the sample through a 4F lens system. The beam splitter directs a fraction of the reflected beam to focus on the photodiode through a converging lens. Image adapted from [12].

B. Sample Preparation and Mounting

Samples must be fixed and centered on a circular glass slide with epoxy. In order to prevent depth aberrations, samples may be sanded smooth. Once the sample is prepared, the glass slide is placed on an adjustable mount using a custom spanner wrench. The mount is then placed on the microscope, after which point the user can manually focus the laser light by sliding the adjustable mount or turning the fine focus knob. Optimal focus can be achieved by temporarily removing the tube surrounding the photodiode, and adjusting the sample positioning until the laser focuses to a point on the photodiode.

To position the image and verify that the microscope has been properly focused, the user can run an overview image with large dimensions and low sampling frequency to locate the region of interest. The VI has the option to recenter the point onto features the user wishes to capture. The VI takes input from the user to move in the X and Y directions, giving the user full control of positioning. By adjusting the focus of the lens itself, the microscope can also be positioned in the z direction as well.

C. Motorized Mirror Control System

The mirror control system is operated by two stepper motors, one for each degree of freedom of the mirror. Both motors are controlled by the LabVIEW VI and NI-DAQmx card, shown schematically in Figure 2. Digital counters on the NI-DAQmx generate electric pulses that allow the motor to step clockwise or counterclockwise. The direction of the motors is determined by the user and is set by two different ports on the NI-DAQmx card.

As part of our testing, we determined the reliability and limitations of the stepper motors. We tested our stepper motors through a range of operating frequencies and determined that the motors are capable of completing 10 rotations, the equivalent of 7680 motor steps,
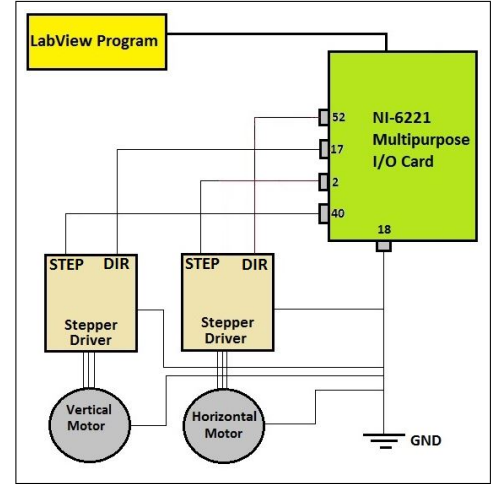

FIG. 2. **High Level Schematic of Motor Control Interface:** The stepper drivers are controlled from the LabVIEW Program using NI-6221 DAQ. Relevant control signals are STEP (the number of steps to turn) and DIR (clockwise or anticlockwise direction). Pin 18 is used as ground.

without jamming or failing at step rates of up to 15 kHz when operated independently of the microscope assembly. When connected to the scanning mirror, the motors can run reliably at frequencies of up to 2000 Hz, or up to 2500 Hz for exploratory scans lasting under about a minute in length. On the microscope, the motors have a finite range of motion that is set by the length of the screws that fix the motors to the mechanical assembly. Before a scan takes place, the screws connected to the motors must be manually adjusted by the user so that approximately 3 mm of the screw is exposed from the base. Both the horizontal and vertical motors can be turned approximately 5000 steps in either direction before the screw jams or loosens and must be reset. To prevent jamming, our program centers the laser back to its initial position on the sample after each run.

D. Signal Detection

The reflected light from the sample is directed towards the photodiode, causing a change in its resistance. The change in resistance causes a voltage change across the terminals of the photodiode. An active low-pass filter amplifies this voltage change while eliminating noise as shown in Figure 3.

The operational amplifier shown in Figure 3 amplifies the difference in voltage at its two terminals. The non-inverting input is grounded while the inverting input is connected to the photodiode. The feedback path from the output to the input, consisting of resistor and capacitor, acts as a low-pass filter to eliminate high frequency noise.
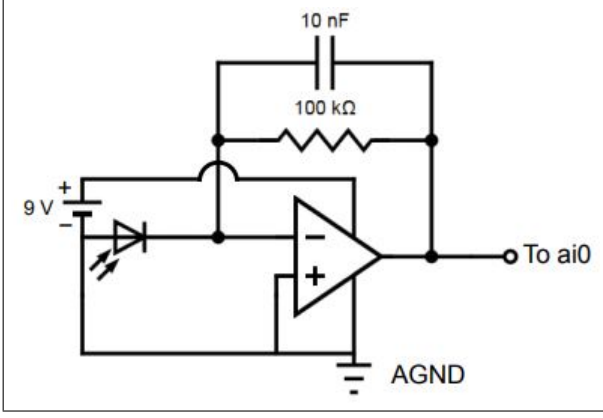
FIG. 3. **Photodiode Circuit:** The output of the circuit is connected to an analog input pin on NI-DAQmx while AGND is connected to analog ground on NI-DAQmx. The op-amp was powered using a 9 V battery. Image adapted from [12].

E.   Scanning and Synchronization

The front panel of the VI, shown in Figure 4, gives the user full control over the size, spatial dimensions, and scanning speed of the image. The user may also input parameters to move the next scan to a desired location. In order to ensure that the sub-VIs receive integer-valued inputs, some of the user inputs may be rounded slightly in order to prevent errors; in these cases, the values actually used by the VI are displayed next to desired values. The rounding operations, as well as the motor movement and scanning operations, are showcased in the VI block diagram in Figure 5. The microscope block diagram additionally includes a case structure that specifies when and where to save image data, upon user request. A detailed block diagram of the scanning-imaging synchronization sub-VI is shown in Figure 6 in order to more clearly demonstrate the process's timing structure.

Our ADC program is synchronized with the motor motion through a shared hardware timed clock pulse with frequency f_0 set by the user. This clock directly determines the step rate f_0 of the motor; based on the user's input, the hardware clock will be downsampled to the appropriate frequency f_s for taking samples. The program accomplishes this by taking in an input for the number of steps per sample point N. By sampling the hardware clock and outputting a HIGH pulse for every Nth pulse of the hardware clock, the resulting sampling frequency f_s is equal to f_0/N. The motor frequency f_0 is always an integer multiple of the sampling frequency f_s.

There are two methods of scanning images in two dimensions, referred to herein as backrolling and snaking. In theory, each of these methods produces equivalent scans and differ primarily in the scanning protocol. In both methods, the microscope begins by scanning along one line in the horizontal direction, then stepping up vertically to the next line. In backrolling, which we have

implemented in our program, the motor moves horizontally backwards to return the microscope to the initial horizontal position before beginning the next line scan. In contrast, for snaking the scanning begins as soon as the motor starts moving backwards horizontally along the next line.

The snaking method has the advantage of reduced scan times as there is no pause in scanning during the transition to the next line. However, the backrolling method avoids the problem of motor backlash, which is discussed in more detail in Section V below.

III.   CALIBRATION AND SPATIAL RESOLUTION

The calibration factor ξ of the microscope is the distance moved across the sample per unit step of the motor. Our methodology to determine the calibration factor was to use various samples with known grid spacing and average the results. For example, one sample we used was a TEM grid with high reflectivity contrast and periodicity of $d = 62\mu m$. The TEM grid is a reliable sample for making calibrations, since they are chemically etched to sub-micrometer precision. A sample scan for this particular TEM grid is shown in Figure 7.
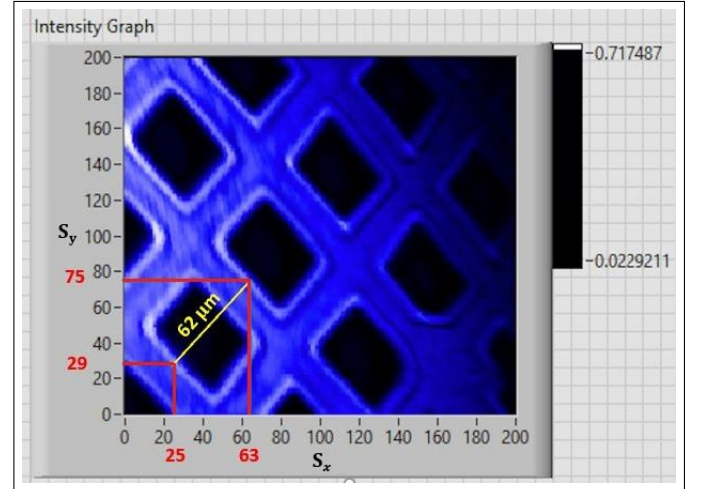

FIG. 7. **TEM Grid:** Uncalibrated intensity plot with number of sample points S_y and S_x in the y and x directions respectively. The sample used had a periodicity of $d = 62\mu m$. We used cursors to accurately determine the number of sample points x and y directions.

To determine the calibration factor ξ, the microscope was scanned across the sample by a fixed number of horizontal and vertical motor steps (N_x, N_y). The sampling frequency was set at $f = 12$ steps/point to obtain the intensity plot shown in Figure 7.

The sample grid lines were identified with high reflected light intensity. Using cursors, the number of sample points across one unit cell were $\Delta S_x = 38$ and
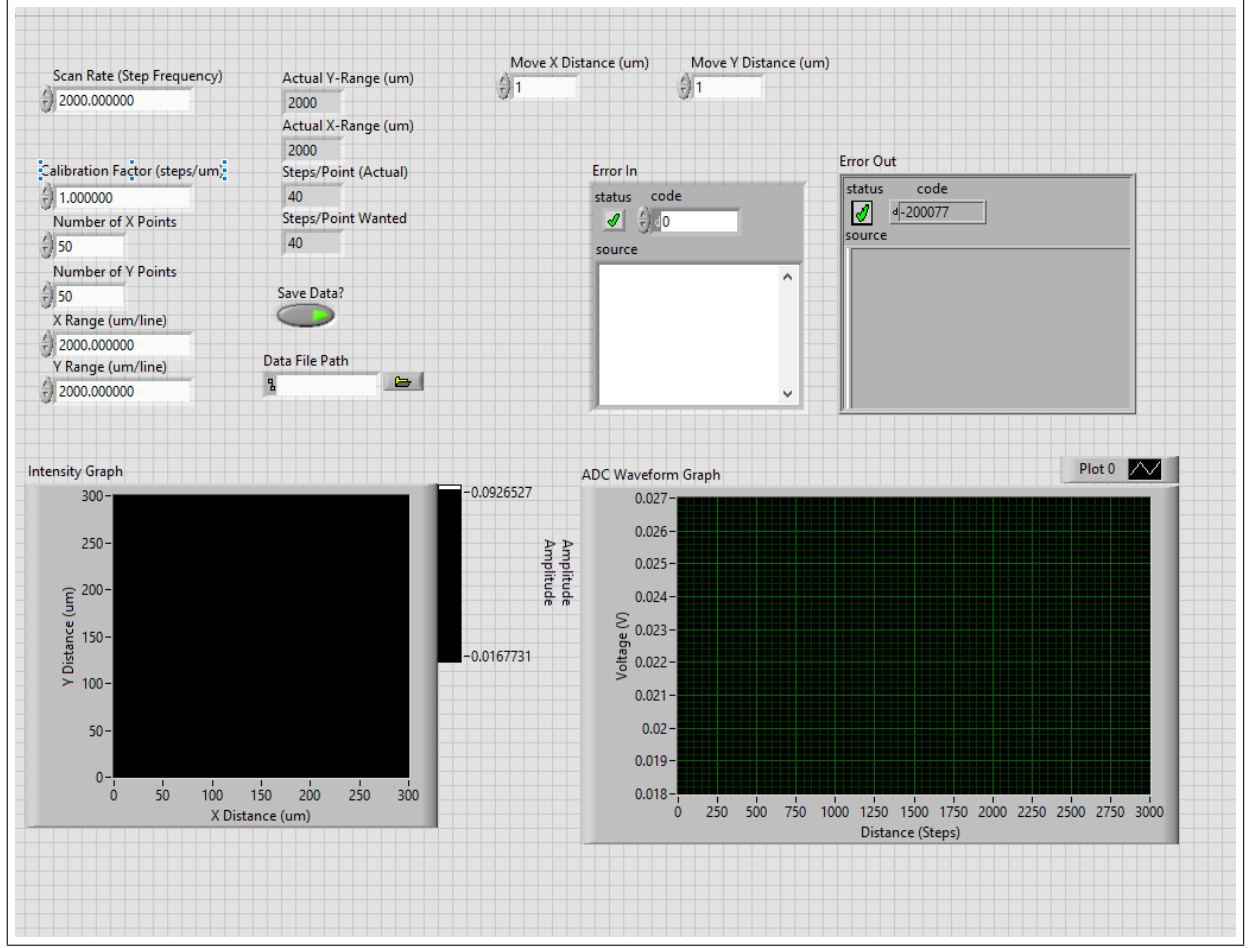
FIG. 4. **Front Panel GUI of Microscope VI** In order to take scans, the user inputs desired parameters into the GUI shown above. Calculations are made in order for the range and step/point values run through the VI to assume integral values; the actual values used in scans are thus shown. As the scan progresses, the intensity graph shows the 2D scan as it grows in size, while the ADC waveform graph shows the most recent line scan. The user may choose to save scan data, and subsequently where to save it to, using the Boolean 'Save Data?' and 'Data File Path' controls, respectively.

$\Delta S_y = 46$, as shown in Figure 7. Given a sampling frequency of $f = 12$ steps/sample, the number of motor steps moved in the x and y directions were:

$$\Delta N_x = 12 * \Delta S_x = 456,$$
$$\Delta N_y = 12 * \Delta S_y = 552. \tag{1}$$

From (1), the average number of steps moved in the direction of lattice vector (shown by the yellow line in Figure 7) is given by:

$$\langle N \rangle = \sqrt{\Delta N_x^2 + \Delta N_y^2} = 716.$$

Therefore, the calibration factor ξ for this image, in μm per step, is given by:

$$\frac{1}{\xi} = \frac{62}{716}\frac{\mu m}{steps} = 0.087\frac{\mu m}{step}. \tag{2}$$

This value was confirmed by taking measurements of many TEM grids with separate opto-mechanical assem-

blies, leading to the equivalent calibration factor of

$$\xi = 12 \pm 2\frac{steps}{\mu m}.$$

Using the calibration factor ξ, the front panel allows the user to simply input the x and y ranges in μm for the scanning area. These distances are automatically be mapped to the number of steps to be moved by the vertical and horizontal motors, allowing the axes of final images to be in calibrated units of length.

The theoretical limit on the spatial resolution of an imaging system such as ours is given by the Rayleigh Criterion,

$$r = \frac{0.61\lambda}{NA},$$

where λ is the wavelength of light employed in the imaging process and NA is the numerical aperture of the lens.

With a red diode laser ($\lambda = 670$ nm) and lens with $NA = 0.65$ used in our microscope, the minimum spatial resolution is approximately $= 0.63\mu m$. The motor
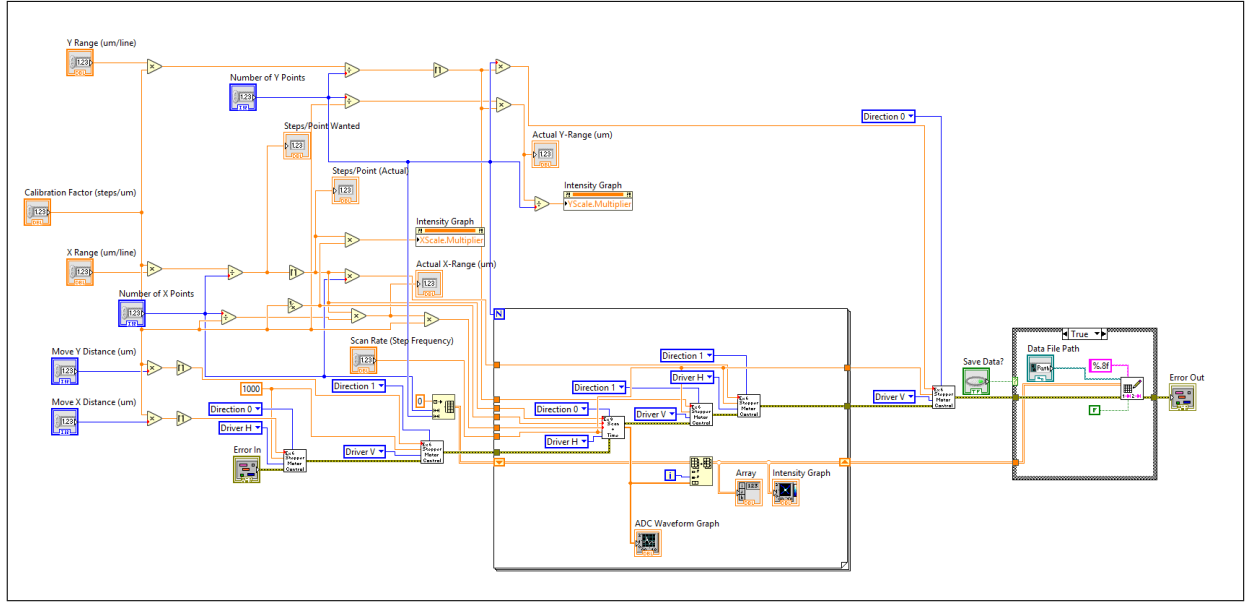
FIG. 5. **Block Diagram of Microscope VI** The microscope VI takes several user inputs, such as scanning speed, image size, and steps/point. After performing preliminary calculations to ensure that all operational parameters assume integral values, the user inputs are passed to motor movement and synchronization sub-VIs that capture and present an image of the sample. Data is passed to graphs on the front panel in real time for immediate viewing, and can be saved to a designated folder when the scan is complete.
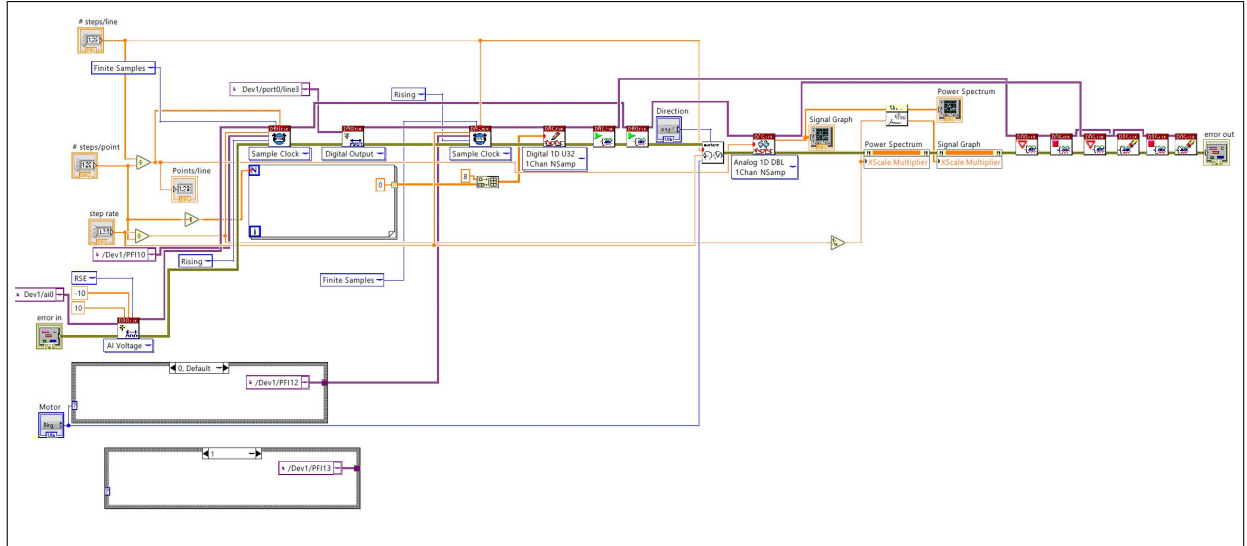

FIG. 6. **Block Diagram of Scanning Synchronization sub-VI** The motors are controlled by a digital counter that takes direction and step rate as inputs. The motors are synchronized with ADC using a hardware timed clock that downsamples the signal from the counter to the appropriate sampling frequency.

step precision $1/\xi$ given in (2) is much less than this value; therefore, the spatial resolution is lower bounded by the optical constraints as opposed to the mechanical constraints of our microscope.

In order to determine the true spatial resolution of the microscope, we rely on the assumption that the TEM grid images jump discretely from high to low reflectivity over boundaries. In practice, the grid boundaries are smaller than the laser spot size due to precision etching, which gives merit to our assumption.

To find the experimental spatial resolution, we first imaged a TEM grid boundary using a steps/point value of 3. We then rotated the image so that the TEM border was vertical, then averaged 100 linescans in order to reject noise. The result of this process is shown in Figure 8, wherein a clear drop-off in intensity can be seen. We then found the distance between points that had intensity values within 10% of the maximum and minimum
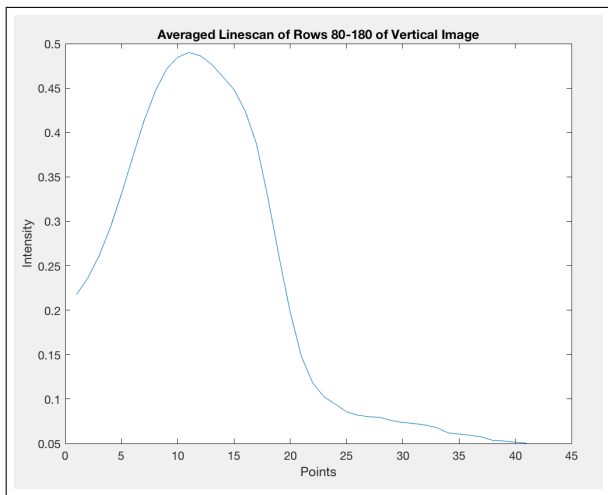
FIG. 8. ***Spatial Resolution Determination:*** Approximately 100 linescans were averaged in order to reduce noise and see an accurate representation of the microscope's ability to detect discrete transitions in reflectivity. In this linescan, the intensities at points X = 15 and X = 25 are within 10% of the maximum and minimum reflectivities, respectively, which leads to the spatial resolution of approximately $2.5\mu m$ determined above.

intensities, and used the calibration factor ξ to determine that our microscope has a proper spatial resolution of $2.5 \pm 0.4\mu m$, a value approximately 4 times larger than the theoretical limit.

The discrepancy between the theoretical and experimental values of spatial resolution can possibly be ascribed to mechanical vibrations, motor imperfects, unfocused light, the lack of a truly discrete transition in spatial reflectivity, or other systematic imperfections in the system. Still, our experimental resolution is within an order of magnitude of the theoretical limit of such a system, and we expect that refinements in technique and procedure may lead to considerably higher image resolutions.

IV. EXAMPLE MEASUREMENTS ON THE MICROSCOPE

In this section, we present two sample images taken with the microscope described herein. These samples possess surface features with sizes on the order of microns. Our first sample was a TEM grid, shown in Figure 7, which was also used to calibrate the microscope. The TEM grids are chemically etched to standardized dimensions and have high reflectivity, especially towards the edges. The TEM grid was also used to test the limits of the image size, which is approximately 400 μm by 400 μm.

We imaged a cross section of an old transistor, as shown in Figure 9. The central component of the transistor consists of several wires and metal grooves that are micrometer-sized, some of which we were able to capture. Because the microscope captures reflectivity instead of real color, the image displays contrast between the reflective metallic pieces of the transistor and the silicon substrate underneath.

V. DISCUSSION

As mentioned before, we wrote our program to implement the scan using backrolling as opposed to snaking, due to the latter's backlash problem. Backlash refers to lost motion incurred when the direction of movement is reversed [10]; in our case, this refers to the reversal of the horizontal motor's direction during transitions between lines. The motor backlash causes successive line scans to be shifted by a certain number of steps from the previous ones. Figure 10 shows the juxtaposition of two scanned images of the same TEM grid, using snaking and backrolling methods, respectively.
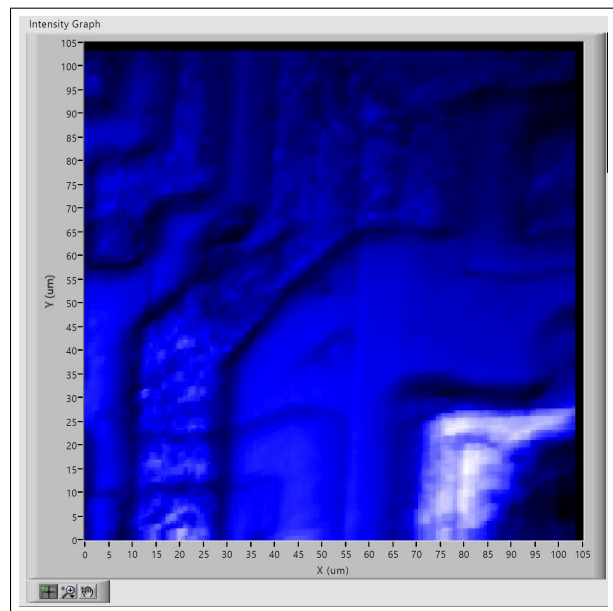

FIG. 9. ***Transistor:*** A calibrated image of the transistor with features visible above the substrate. A reflective chip is imaged in the lower right corner.

In theory, the offset from the backlash effect can be quantified and corrected for in the final data[11]. In practice, however, it is a painstaking task for non-experts in the field of mechanics. One reason for this is that the correction offset usually occurs by an arbitrary number of steps which can vary across different line scans. Therefore, we find the backrolling method to be the most suitable scanning method for our microscope.

One of the advantages of the microscope is its ability to capture reflectivity contrast between different features on a submicron scale. This is particularly useful in semiconductor heterostructures, where differences in material reflectances can be readily exploited to give a high-contrast
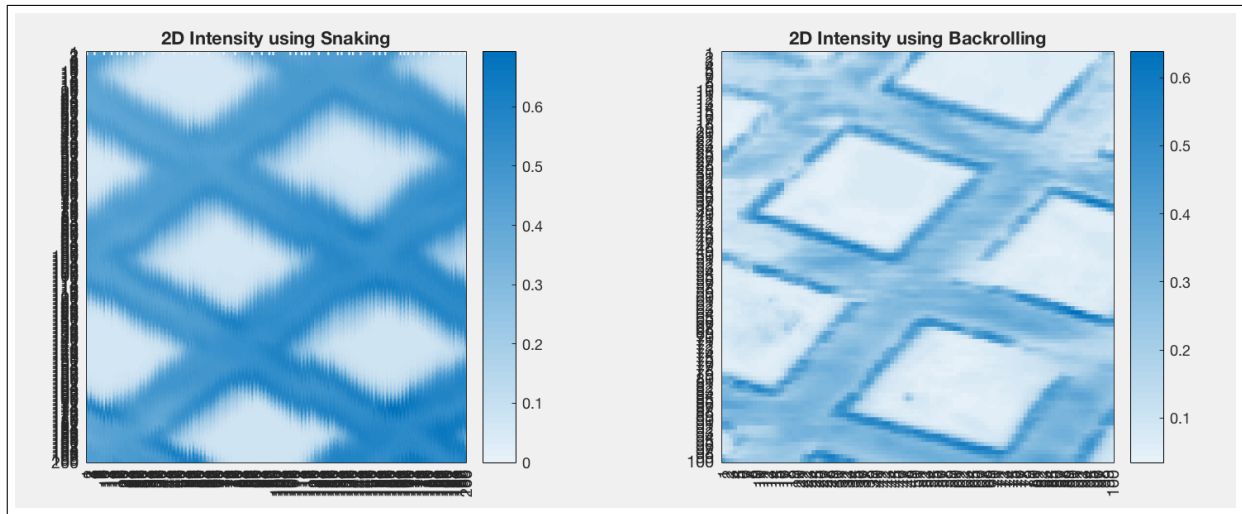
FIG. 10. **Snaking vs. Backrolling:** A 200-by-200 point image of a TEM grid taken using the snaking protocol on the left is compared to a 100-by-100 point image using the backrolling method. It can be observed that snaking leads to shifted linescan intensities in every other column due to backlash, while the image taken using backrolling has no such phenomenon.

image. In our transistor scan, for example, we were able to distinguish between the wires and grooves. In our TEM scan, we were able to clearly distinguish the edges of the more reflective grids from the background substrate material. The reflectivity of the TEM grid edges allows us to observe individual features on the grid itself, including scratches and etches made on the edges. Such high resolution can be effectively used for studying the variation of surface features in a sample. For example, our scanning laser microscope can employed for finding defects on the surface of a microelectronic device or on a biological tissue.

One limitation of our instrument is that the microscope requires manual re-positioning when a feature is located on a sample. There is no means to return to a previous spot following a readjustment. As a result, the microscope is impractical for studying features larger than the scanning region or separated far apart. The scanning time of the microscope scales roughly linearly with the number of points. This is effective for smaller scan regions, though this also means larger 2D scans will scale as the square of the line size. Typical scan sizes of a tenth of a millimeter can be completed with a high sampling rate within an hour.

The steering motors also pose a physical limitation to the microscope, since they have a finite range of motion in each scanning direction. After extended use, the motors heat up, which can cause thermal expansion of the plastic tubing connected to the motors. This may adversely impact transfer of motion from the motors to the steering mirror's knobs. Therefore, it is inadvisable to run multiple consecutive runs for a long period of time.

VI. CONCLUSIONS

In totality, we have demonstrated the construction and use of a scanning laser microscope. Using a NI-DAQmx, we created a working VI that controls the electric signals sent to the microscope to power the motors and scanning routine. By verifying the functionality of our microscope by modular testing as well as by running several test scans, we have determined that our microscope is fully capable of imaging both electronic and biological samples at high fidelity and repeatability. Additionally, by calibrating the microscope with a TEM sample mount, the microscope described herein is capable of displaying the spatial reconstruction of any given sample. Furthermore, the user has access to the raw image data, which enables the application of several image processing techniques to further increase resolution for desired applications.

The laser scanning microscope is a fully functioning and self-contained apparatus that gives the user precise, accurate and consistent scans with micron resolution. With further improvement planned by our group and by the scientific community as a whole, we believe this microscope will serve as a valuable asset to those who are limited to using more expensive alternatives in various realms of research and engineering.

[1] R. H. Webb, Rep. Prog. Phys. **59**, 427 (1996).
[2] M. Li, S. K. Cushing, and N. Wu, Analyst. **140**, 386 (2015).
[3] Y. Lee, K. Hoshino, A. Alù, and X. Zhang, Optics Express **21**, 2748 (2013).
[4] S. Krishnan, P. Diagaradjane, and S. H. Cho, Int J Hy-

perthermia **26**, 775 (2010).

[5] W. Sun, Q. He, S. Sun, and L. Zhou, Light: Sci. & Appl. **5**, e16003 (2016).

[6] W. B. Amos and J. G. White, Biology of the Cell **95**, 335-342 (2003).

[7] N. G. Horton, K. Wang, D. Kobat, C. G. Clark, F. W. Wise, C. B. Schaffer, and C. Xu, Nature Photonics **7**, 205 (2013).

[8] M. Gunkel, F. Erdel, K. Rippe, P. Lemmer, R. Kaufmann, C. Hörmann, R. Amberger, and C. Cremer, Biotechnol. J. **4**, 927 (2009).

[9] 6 J.-M. Segura, A. Renn, and B. Hecht, Rev. Sci. In-

strum. **71**, 1706 (2000).

[10] Backlash. Retrieved September 2, 2018 from `https://www.webcitation.org/5nQCqsUa9?url=http://www.qtcgears.com/Q410/PDF/techsec14.pdf`

[11] Understanding Backlash and Stiction (Motion Control and Motor Association) Retrieved December 8, 2018 from `https://www.motioncontrolonline.org/content-detail.cfm/Motion-Control-Technical-Features/Understanding-Backlash-and-Stiction/content_id/310`

[12] J. Moses and G. Fuchs, *Interfacing the Digital Domain with an Analog World: AEP 2640*, (2018)